COMMUNICATION

Check for updates

Interfacial dipole engineering in all-inorganic perovskite solar cells†

Kuidong Gao,[a] Lei Gao,[a] Qiurui Wang,[a] Yijie Chang,[a] Qiang Zhang,[a] Yuanyuan Zhao*[a] and Qunwei Tang ⓘ *[b]

Severe nonradiative recombination and energy level mismatch in perovskite solar cells (PSCs) are key factors affecting efficiency. Here, we report an effective strategy for surface passivation and interfacial dipole engineering of perovskite films. By precisely introducing electron-withdrawing and electron-donating groups on 7-azaindole, we have effectively controlled the passivation ability of N atoms and the polarity of the interfacial dipole, thereby regulating the perovskite surface's work function and obtaining the optimal energy level matching. This strategy yields an impressive efficiency of 10.76% for the $CsPbBr_3$ PSC and exceptional stability.

Organic–inorganic halide perovskite solar cells (PSCs) have garnered significant attention, achieving a record-breaking power conversion efficiency (PCE) of 26.1%.[1–3] However, their stability falls below commercial requirements when exposed to moisture, heat, and light, primarily due to the degradation of organic groups like MA^+ and FA^+.[4] To overcome these challenges, all-inorganic $CsPbX_3$ ($X^- = I^-$, Br^-, Cl^-, or mixed) perovskites have emerged as a promising solution.[5,6] While iodide-containing perovskites offer more suitable bandgaps, their black-phased structure easily transforms into non-perovskite yellow phases, hampering progress in iodide-containing all-inorganic PSC research.[7] On the other hand, iodide-free $CsPbBr_3$ perovskite exhibits excellent weatherability and a wide bandgap of 2.3 eV, making it highly promising for next-generation photovoltaic technologies, tandem solar cells, and high-voltage electronics.[8] However, $CsPbBr_3$ PSCs have achieved a reported PCE of 11.21%, which is still significantly below its theoretical efficiency limit.[9]

Solution-processed perovskite films are prone to generating defects at surfaces and grain boundaries, which act as nonradiative

recombination centers, leading to decreased open circuit voltage (V_{oc}) and fill factor (FF) in $CsPbBr_3$-based PSCs. This leads to undesired energy loss.[10,11] Furthermore, proper energy level alignment at the interface is crucial for minimizing energy losses.[12] Therefore, an effective strategy to mitigate energy loss and enhance device PCE involves repairing surface defects and promoting energy level alignment.

Surface defects are addressed using Lewis base molecules and polymers. These passivators, containing N, O, or S atoms, reduce uncoordinated Pb^{2+} ions and defects at the film surface and grain boundaries.[13,14] Recent investigations have revealed that the introduction of electron-donating methoxyl ($-OCH_3$) and electron-withdrawing nitryl ($-NO_2$) on the benzene ring can effectively regulate the passivation ability of molecules.[11,15] Directly regulating the electron density of passivation sites, independent of the benzene ring, is a critical focus for future research. While passivators effectively reduce defects, limited charge extraction efficiency at interfaces remains a barrier to enhancing device performance.

Asymmetric molecules possess a dipole moment created by positive and negative charge centers. This distribution of charges alters the work functions (WFs) and strongly influences charge carrier transport at the interface.[16] For instance, Zhang et al. introduced donor–π–acceptor (D–π–A) dipoles at the perovskite/electron transport layer (ETL) interface, enhancing the built-in electric field and lowering the WF.[17] Wu et al. incorporated two new naphthalimide-based molecules (PX, X = F, I) into the perovskite layer, creating an interfacial electrical dipole layer that enhances hole extraction and reduces the WF.[18] Because the direction and intensity of surface dipoles depend on specific molecule-to-surface interactions, which cause an increase and decrease of the WF, precisely controlled dipoles will determine the energy level matching, which can help influence carrier-oriented extraction transfer kinetics.

In this work, we developed a strategy for surface passivation and cooperative construction of interfacial dipoles. By investigating three different 7-azaindole (7-AI) derivatives, we

[a] College of Mechanical and Electronic Engineering, Shandong University of Science and Technology, Qingdao 266590, PR China. E-mail: yuanyuanzhao@sdust.edu.cn

[b] Institute of Carbon Neutrality, College of Chemical and Biological Engineering, Shandong University of Science and Technology, Qingdao 266590, PR China. E-mail: tangqunwei@sdust.edu.cn

discovered that the electron-donating –OCH$_3$ increased the electron cloud density, reducing surface defects and nonradiative recombination. Conversely, the electron-withdrawing –NO$_2$ showed weaker passivation. Through the adjustment of the functional group, we successfully modulated the WF of the perovskite film. The negative interfacial dipole decreased the WF, while the positive dipole increased it. Remarkably, the 7-AI-OCH$_3$ achieved excellent energy level alignment, enabling efficient hole extraction and transfer. This approach reduced nonradiative recombination. The synergistic effects of Lewis base passivation and the driving force for charge extraction and transfer resulted in an impressive champion PCE of 10.76% for the CsPbBr$_3$ PSC based on 7-AI-OCH$_3$. This PCE is among the highest efficiency levels for congeneric PSCs (Table S1, ESI†). Furthermore, the unpackaged PSC exhibited excellent stability.

To directly modulate electron density at passivation sites, we employed different electronegative functional groups. Notably, we chose 7-AI derivatives, namely 7-AI-NO$_2$, 7-AI, and 7-AI-OCH$_3$, for the first time in PSCs. Using density functional theory (DFT), we analyzed the electrostatic potential (ESP) distributions (Fig. 1a). The –OCH$_3$ significantly increases the electron cloud density on the azaindole ring, especially at the N atom, and the –NO$_2$ produces the opposite effect. Thus, electron-donating functional groups hold promise for enhancing defect passivation effects.[19]
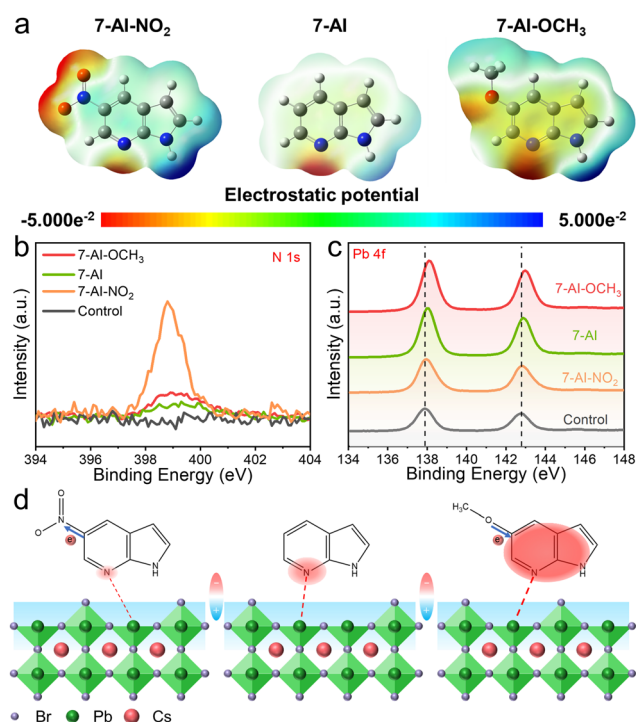

Fig. 1 (a) Molecular structures and electrostatic potential maps of 5-nitro-7-azaindole (7-AI-NO$_2$), 7-azaindole (7-AI), and 5-methoxy-7-azaindole (7-AI-OCH$_3$). XPS spectra of (b) N 1s and (c) Pb 4f in CsPbBr$_3$ films without and with organic molecule treatment. (d) Schematic diagram of electron-transfer-induced coulomb force regulation and the N atom passivated uncoordinated Pb^{2+}.

To confirm the presence of 7-AI derivatives on perovskite films rather than volatilization or sublimation, X-ray photoelectron spectroscopy (XPS) analysis reveals that the control sample does not exhibit an N 1s peak (Fig. 1b), whereas perovskite films modified with 7-AI derivatives show N 1s peaks, confirming the presence of 7-AI derivatives on the perovskite film. Moreover, EDS mapping images (Fig. S1, ESI†) also show the uniform distribution of 7-AI derivatives. Remarkably, the 7-AI-NO$_2$ group exhibits a stronger intensity in the N 1s peak, likely due to the presence of the N element in –NO$_2$.

Additionally, we conducted an analysis of the Pb 4f characteristic peaks (Fig. 1c). Compared to the control CsPbBr$_3$ film, we observed shifts of 0.04, 0.10, and 0.20 eV in the Pb 4f peaks for 7-AI-NO$_2$, 7-AI, and 7-AI-OCH$_3$-passivated CsPbBr$_3$ films, respectively.[11,16] Fourier transform infrared spectroscopy (FTIR) analysis (Fig. S2, ESI†) revealed a low wavenumber shift in the stretching vibration peaks of C=N and C–N, indicating a chemical interaction between the N donor and Pb^{2+} ions. Thus, by modulating the different functional groups, we can alter the coordination ability of N atoms and directly control the electron density at the passivation site. Consequently, N atoms with high electronegativity can suppress positive charge defects (Fig. 1d). Additionally, X-ray diffraction (XRD) patterns (Fig. S3, ESI†) reveal consistent characteristic peaks without any intermediate.

The passivation of surface defects by 7-AI derivatives is expected to reduce trap states, mitigate nonradiative recombination, and minimize energy loss. To investigate these effects, we fabricated some samples with a structure of FTO glass/perovskite for confocal photoluminescence (PL) mapping, PL spectra, and time-resolved photoluminescence (TRPL) spectra (Fig. 2a–c). As the passivation ability of 7-AI derivatives strengthens, PL mapping (Fig. 2a) shows a significant increase in the number of photons (red color). This is consistent with the increase in PL intensity observed in the PL spectra (Fig. 2b), which is attributed to weakened non-radiative recombination in the perovskite film due to the passivation effect of 7-AI derivatives. Furthermore, the more uniform distribution in PL mapping clearly demonstrates the passivation of surface defects on the perovskite film by 7-AI derivatives. TRPL analysis (Fig. 2c and Table S2, ESI†) demonstrated that perovskite films modified with 7-AI derivatives exhibited longer carrier lifetimes compared to the control, thereby facilitating carrier extraction.[18]

The trap density (N_t) of the CsPbBr$_3$ films was assessed through space-charge limited current (SCLC) measurements in pure electronic devices (Fig. 2d and Table S3, ESI†). The N_t, which is proportional to the trap-filled limit voltage (V_{TFL}), decreased, indicating a reduction in surface defects. Furthermore, we directly determined the built-in potential (V_{bi}) by analyzing the capacitance–voltage (C–V) curves using the Mott–Schottky equation (Fig. 2e). Notably, the 7-AI-OCH$_3$ modified device exhibited a higher V_{bi} (1.326 V) compared to the control (1.261 V), 7-AI-NO$_2$ (1.297 V), and 7-AI (1.318 V), indicating suppressed nonradiative recombination and a higher V_{oc} output.[20]

Fig. 2 (a) Confocal PL mapping images, (b) PL spectra, and (c) TRPL spectra of the control and 7-AI derivative modified perovskite films directly deposited on the glass substrate. (d) SCLC curves of the electron-only device with a structure of FTO/SnO$_2$–TiO$_x$Cl$_{4-2x}$/perovskite/PCBM/carbon without and with 7-AI derivative treatment. (e) Mott–Schottky (M–S) of various devices with a structure of FTO/SnO$_2$–TiO$_x$Cl$_{4-2x}$/perovskite/carbon.

Fig. 3 (a) Calculated dipole moment images of the three molecules. Schematic illustration of charge carrier collection and recombination in (b) 7-AI-NO$_2$-based PSCs and (c) (AI or AI-OCH$_3$)-based PSCs. (d) The architecture and cross-sectional SEM image of all-inorganic CsPbBr$_3$ PSCs. (e) The J–V curves, (f) IPCE spectra, and (g) steady power output curves of various CsPbBr$_3$ PSCs.

Although V_{bi} facilitates improved V_{oc} output,[21] the energy level mismatch may also lead to an undesired loss of V_{oc}. By combining ultraviolet-visible (UV-vis) absorption spectra (Fig. S4, ESI†) and ultraviolet photoelectron spectroscopy (UPS) (Fig. S5, ESI†), we obtained energy levels and band structure data for the perovskite films (Fig. S6 and Table S4, ESI†). Notably, the modification of 7-AI led to a reduction in the WF of the perovskite film, with a further decrease in the WF observed for the 7-AI-OCH$_3$, while the WF increased for the 7-AI-NO$_2$, surpassing the control. To elucidate the factors influencing the change in WF, we calculated the dipole moment of the 7-AI derivatives. As shown in Fig. 3a, the electron-donating –OCH$_3$ enhances the dipole moment of 7-AI, resulting in a negative dipole, while the electron-withdrawing –NO$_2$ induces a pronounced redistribution of electron density within the ring, resulting in a positive dipole. When the N atom coordinates with the uncoordinated Pb^{2+} ions, the 7-AI derivatives align side by side at the interface, forming an electric dipole layer, which exerts an influence on the vacuum energy level (E_{vac}) and WF according to the equation $\Delta = nep/\varepsilon_0\varepsilon$, where e represents the elementary electron charge, n denotes the density of the electric dipole, p signifies the dipole moment, and ε and ε_0 represent the dielectric constant of the dipole material and vacuum permittivity, respectively.[18] As p is a vector, its magnitude determines the magnitude of Δ, and its direction determines the sign of Δ. A positive dipole results in a positive Δ, while a negative dipole leads to a negative Δ. Consequently, the WF

increased for 7-AI-NO$_2$, while it decreased for 7-AI and 7-AI-OCH$_3$, consistent with previous findings.[11,18–20]

Additionally, Kelvin probe force microscopy (KPFM) cross-validated the WF change (Fig. S7, ESI†). The results indicate that perovskite films treated with negative dipolar molecules exhibit a higher contact potential difference (CPD, defined as the potential difference between sample and tip), while positive dipoles show the opposite trend, following the sequence of 7-AI-OCH$_3$ > 7-AI > control > 7-AI-NO$_2$. It is noted that the same type of conductive tip was used in the measurements of KPFM to make Φ_{tip} (WF of the tip) consistent. According to the equation: CPD = $(\Phi_{tip} - WF)/e$, a high CPD of 7-AI-OCH$_3$ and 7-AI means a low WF of the sample, a low CPD of 7-AI-NO$_2$ means a high WF of the sample.[22] Notably, 7-AI-NO$_2$ had a lower valence band minimum (VBM) and conduction band minimum (CBM) compared to the control, hindering energy level alignment and increasing the aggregation and recombination of carriers at the interface (Fig. 3b). Conversely, 7-AI and 7-AI-OCH$_3$ achieved higher VBM and CBM, facilitating the extraction of holes (Fig. S8, ESI†) and the withdrawal back of electrons at the interface (Fig. 3c).

To examine the influence of 7-AI derivatives on photovoltaic performance, we fabricated carbon-based CsPbBr$_3$ PSCs (Fig. 3d). Initially, we optimized the concentration of the modified molecules (Fig. S9–S11 and Tables S5–S7, ESI†). Interestingly, the presence of a high concentration of 7-AI-NO$_2$ has a detrimental effect on the photovoltaic performance, which is attributed to an energy level mismatch that outweighs the positive effect of passivation. The champion device, modified with 7-AI-OCH$_3$, exhibits an impressive PCE of 10.76% with a V_{oc} of 1.675 V (Fig. 3e). This represents a remarkable

Fig. 4 Long-term stability of the inorganic CsPbBr$_3$ PSCs at (a) RH = 80%, T = 25 °C and (b) RH = 0%, T = 80 °C. The water contact angle of (c) control and (d) 7-AI-OCH$_3$-based perovskite films.

24.68% enhancement in PCE compared to the control (8.63%). The improvement of device photovoltaic performance attributed to 7-AI derivatives is also applicable to other components of PSCs. For instance, carbon-based CsPbI$_2$Br PSCs achieved a champion PCE of 14.24% (Fig. S12, ESI†). The augmented PCE is further confirmed by the incident photon-to-electron conversion efficiency (IPCE) spectra (Fig. 3f), steady-state power output (Fig. 3g), and statistical photovoltaic data (Fig. S13, ESI†). The notable improvement in photovoltaic performance can be attributed to both efficient passivation of defects and better energy level alignment, minimizing nonradiative recombination and enhancing hole extraction.

Moreover, electrochemical impedance spectroscopy (EIS) measurements were employed to investigate the interfacial charge transfer and recombination in the devices (Fig. S14a, ESI†). The results demonstrate that the modification of 7-AI derivatives enhances the recombination resistance (R_{rec}), effectively suppressing carrier recombination and reducing leakage current (Fig. S14b, ESI†) Furthermore, the V_{oc} decay curves (Fig. S15, ESI†) reveal a prolonged electron lifetime, indicating an increased likelihood of efficient extraction.

Finally, long-term stability was tested on unencapsulated CsPbBr$_3$ PSCs, monitoring the photovoltaic parameters over a 30 day period at room temperature and 80% RH, as well as under vacuum at 80 °C (Fig. 4a, b and Fig. S16, ESI†). The results show outstanding stability, attributed to the hydrophobicity of 7-AI-OCH$_3$ (Fig. 4c and d) and the defect passivation.

In summary, we have developed a strategy for surface passivation and cooperative construction of interfacial dipoles. The 7-AI derivatives have proven to be effective in passivating surface defects, thereby reducing trap states and nonradiative recombination. Notably, the N–Pb bond at the interface creates an electric dipole layer. The introduction of electron-donating –OCH$_3$ enhances the negative dipole, resulting in a lower WF of the perovskite films. Conversely, the electron-withdrawing –NO$_2$ alters the electron density distribution within the 7-AI ring, leading to a positive dipole and an increased WF. Importantly, 7-AI-OCH$_3$ achieves optimal energy level alignment,

facilitating efficient hole extraction and minimizing nonradiative recombination. This strategy results in an impressive efficiency of 10.76% and exceptional stability.

Conflicts of interest

There are no conflicts to declare.

Notes and references

1 A. Kojima, K. Teshima, Y. Shirai and T. Miyasaka, J. Am. Chem. Soc., 2009, 131, 6050–6051.
2 M. Kim, J. Jeong, H. Lu, T. K. Lee, F. T. Eickemeyer, Y. Liu, I. W. Choi, S. J. Choi, Y. Jo, H.-B. Kim, S.-I. Mo, Y.-K. Kim, H. Lee, N. G. An, S. Cho, W. R. Tress, S. M. Zakeeruddin, A. Hagfeldt, J. Y. Kim, M. Gratzel and D. S. Kim, Science, 2022, 375, 302–306.
3 Best research-cell efficiency chart, National Renewable Energy Laboratory (NREL), 2023, https://www.nrel.gov/pv/assets/pdfs/best-research-cell-efficiencies.pdf.
4 K. O. Brinkmann, J. Zhao, N. Pourdavoud, T. Becker, T. Hu, S. Olthof, K. Meerholz, L. Hoffmann, T. Gahlmann, R. Heiderhoff, M. F. Oszajca, N. A. Luechinger, D. Rogalla, Y. Chen, B. Cheng and T. Riedl, Nat. Commun., 2017, 8, 13938.
5 J. Zhang, G. Hodes, Z. Jin and S. Liu, Angew. Chem., Int. Ed., 2019, 58, 15596–15618.
6 A. Ho-Baillie, M. Zhang, C. F. J. Lau, F.-J. Ma and S. Huang, Joule, 2019, 3, 938–955.
7 J. Liang, X. Han, J. H. Yang, B. Zhang, Q. Fang, J. Zhang, Q. Ai, M. M. Ogle, T. Terlier, A. A. Marti and J. Lou, Adv. Mater., 2019, 31, 1903448.
8 Q. Zhou, J. Duan, X. Yang, Y. Duan and Q. Tang, Angew. Chem., Int. Ed., 2020, 59, 21997–22001.
9 R. Guo, J. Xia, H. Gu, X. Chu, Y. Zhao, X. Meng, Z. Wu, J. Li, Y. Duan, Z. Li, Z. Wen, S. Chen, Y. Cai, C. Liang, Y. Shen, G. Xing, W. Zhang and G. Shao, J. Mater. Chem. A, 2023, 11, 408–418.
10 L. Gao, Y. Zhao, Y. Chang, K. Gao, Q. Wang, Q. Zhang and Q. Tang, Chem. Eng. J., 2023, 469, 143881.
11 J. Duan, M. Wang, Y. Wang, J. Zhang, Q. Guo, Q. Zhang, Y. Duan and Q. Tang, ACS Energy Lett., 2021, 6, 2336–2342.
12 J. Chen and N. G. Park, Adv. Mater., 2019, 31, 1803019.
13 L. K. Ono, S. Liu and Y. Qi, Angew. Chem., Int. Ed., 2020, 59, 6676–6698.
14 S.-H. Lee, S. Jeong, S. Seo, H. Shin, C. Ma and N.-G. Park, ACS Energy Lett., 2021, 6, 1612–1621.
15 J. Zheng, J. Chen, D. Ouyang, Z. Huang, X. He, J. Kim and W. C. H. Choy, ACS Appl. Mater. Interfaces, 2020, 12, 57165–57173.
16 Q. Chen, C. Wang, Y. Li and L. Chen, J. Am. Chem. Soc., 2020, 142, 18281–18292.
17 C. Zhang, W. Kong, T. Wu, X. Lin, Y. Wu, J. Nakazaki, H. Segawa, X. Yang, Y. Zhang, Y. Wang and L. Han, ACS Appl. Mater. Interfaces, 2021, 13, 44321–44328.
18 T. Wu, R. Zhao, J. Qiu, S. Wang, X. Zhang and Y. Hua, Adv. Sci., 2022, 9, 2203640.
19 T. Wu, Y. Wang, X. Li, Y. Wu, X. Meng, D. Cui, X. Yang and L. Han, Adv. Energy Mater., 2019, 9, 1803766.
20 Y. Liao, J. Zhang, W. Wang, Z. Yang, R. Huang, J. Lin, L. Che, G. Yang, Z. Pan, H. Rao and X. Zhong, Adv. Funct. Mater., 2023, 33, 2214784.
21 P. Cui, Q. Qu, Q. Zhang, B. Liu, L. Yan, S. Du, X. Wang, H. Huang, J. Ji and M. Li, Energy Mater., 2021, 1, 100014.
22 Y. Lin, Y. Shao, J. Dai, T. Li, Y. Liu, X. Dai, X. Xiao, Y. Deng, A. Gruverman, X. Zeng and J. Huang, Nat. Commun., 2021, 12, 7.